

Learning holographic QCD with unflavoured meson spectra

Mathew Thomas Arun ¹, Ritik Pal²

School of Physics, Indian Institute of Science Education and Research, Thiruvananthapuram 695551, Kerala, India

Abstract

We develop a neural network framework to predict the five-dimensional background geometry, dilaton potential, and chiral symmetry breaking scalar potential of holographic QCD from unflavored meson mass spectra. The model was trained in a discretized form of the Schrödinger-like equation, which resembles a linear moose in “deconstructed” 5 dimensions with Dirichlet boundary conditions, in contrast to the AdS/DL with “emergent” space-time. Using the ρ , a_1 , a_2 , and f_0 unflavored mesons and their excitations as training data, the model learns confining effective potentials and computes a dilaton profile that satisfies the null energy condition. The network predicts the IR behavior of dilaton to be in-between linear and quadratic forms. Moreover, the symmetry-breaking bulk potential of the scalar field, $V(X) = k_1 X^3 + k_2 X^4$, was computed, and the parameters k_1 and k_2 predicted to be ~ -8 and ~ 17 respectively. The deep-learned parameters, metric, and the dilaton profile were then used to predict the pion mass and its spectrum with good accuracy. A Python code, along with the trained models, is provided to facilitate further studies³.

1 Introduction

The AdS/CFT correspondence [1–3] has provided a powerful framework to study strongly coupled gauge theories using classical gravitational theories in higher-dimensional spacetime. One of the most prominent applications of this correspondence is in the study of Quantum Chromodynamics (QCD) through holographic models. The original proposal by Sakai and Sugimoto [4, 5] with $D8/D4/\bar{D}8$ configuration of the branes to achieve chiral symmetry and its spontaneous breaking, despite its success, could not produce massive pions. This geometry was deformed to $D8/D4/\bar{D}8/D6$ [6, 7], to mimic the techni-colour QCD like sector on the $D6$ brane, which successfully provided explicit chiral symmetry breaking through a bare quark mass term arising from the asymptotic distance between the $D4$ and $D6$ branes. While such techni-colour models, for chiral symmetry breaking, have rich phenomenology and were studied in the context of raising the axion mass [8, 9], with the discovery of Higgs, remains disfavoured.

The bottom-up AdS/QCD framework [10–16], in contrast to the string-theoretic approach, remains successful in explaining phenomenological signatures, including the mass spectra of mesons and their decay constants. Unlike full string-theoretic duality, parameters and interactions are chosen to reproduce low-energy QCD observables phenomenologically. These models aim to capture the essential features of QCD, such as confinement and chiral symmetry breaking, by constructing a dual gravitational theory in a 5-dimensional Anti-de Sitter (AdS) space related to the 4-dimensional gauge theory through an effective dictionary. Although the exact gravity dual of QCD and the chiral symmetry breaking dynamics remain unknown, phenomenological models successfully reproduce various hadronic

¹mathewthomas@iisertvm.ac.in

²ritik24@iisertvm.ac.in

³Available at Github, <https://github.com/rp-winter/NN-AdS-QCD>

properties, such as the meson mass spectrum [12, 17–19], which are identified with the Kaluza-Klein (KK) modes of the bulk fields. The dynamics of these bulk fields are governed by Sturm-Liouville-type differential equations, and their eigenvalues correspond to these masses in the dual theory. These equations can often be transformed into Schrödinger-like equations [12], allowing the application of quantum mechanical techniques [20].

There are several proposals for the functional forms of the background fields (such as dilaton profile, warp factor, and scalar vacuum expectation value), each characterized by a few free parameters, which are then fitted to match the hadronic spectra. For example, the Gherghetta-Kaputra-Kelley (GKK) model [17] takes the standard AdS warp factor $A(z) = -\log(z)$, and assumes an ansatz for the bulk scalar vacuum expectation value (VEV) field to reconstruct the dilaton profile. In many improved holographic QCD models, with 5D graviton–dilaton (or graviton–dilaton–scalar) action [21–23], solving the corresponding Einstein-dilaton equations generate a self-consistent warp factor and dilaton profile, instead of an *ad hoc* selection.

Although these models can reproduce the low-lying hadronic spectra with reasonable accuracy, they are often limited by the assumptions made about these background field profiles. Neural networks, being a universal function approximator [24], can be used to approximate these background fields without making any assumptions about their functional forms. There has been an increased interest in the subject with the establishment of a correspondence between the AdS/CFT and Deep Learning (DL) [25], where the deep layers of a deep Boltzmann machine, from the viewpoint of a 4-dimensional QFT at the visible layer, are seen as an “emergent” bulk space coordinate. The trained weights become the metric of the extra-dimensional space-time. Further, the matching of the DL with holographic QCD [26, 27], leverages this correspondence to model the background geometry by fitting the ρ and a_2 mesons using neural networks. This framework was then improved by including a dilaton potential to predict the rho meson spectrum [28].

Meson	State	Experimental Mass (GeV)
ρ	1	0.775 ± 0.023
	2	1.465 ± 0.025
	3	1.57 ± 0.07
	4	1.72 ± 0.02
	5	1.88 ± 0.01
	6	2.044 ± 0.031
a_1	1	1.23 ± 0.04
	2	1.655 ± 0.016
a_2	1	1.318 ± 0.006
	2	1.706 ± 0.014
f_0	1	0.513 ± 0.032
	2	0.99 ± 0.02
	3	1.40 ± 0.04
	4	1.522 ± 0.025
	5	1.733 ± 0.008
	6	1.804 ± 0.016
	7	1.982 ± 0.54
	8	2.187 ± 0.014
	9	2.312 ± 0.007
	10	2.470 ± 0.006

Table 1: Experimental meson masses [47] used for training the neural network.

In this article, we train a neural network model to learn the background geometry of the AdS/QCD model, the chiral symmetry breaking potential, dilton profile and the effective potentials of the mesons by fitting the mass spectrum of the ρ , a_1 , a_2 , and f_0 mesons and all their excitations, given in Table 1. The mass eigenvalues are obtained by solving the Schrödinger-like equation for the bulk modes using a finite-difference discretization, where the spatial coordinate is divided into N points and the second derivative is approximated by a central difference scheme. This leads to a matrix eigenvalue problem, which can often be cast into a real symmetric form and solved using numerical eigenvalue solvers. By minimizing the difference between the predicted and experimental meson masses using gradient descent, we can optimize the neural networks to find the background geometry. The Python code can be found at [29], which can be easily modified to train further models. In contrast with the AdS/DL framework, the neural network model we construct here closely follows the “deconstruction” [30–37] of a warped 5-dimensional theory with Dirichlet boundary conditions [38].

Our results show good agreement with the experimental values for the ρ , a_1 , a_2 , and f_0 meson masses used in training. To test the generalization capability of the trained model, we use the same trained model to predict the excited-state masses of the π mesons, which are in reasonable agreement with the experimental values, demonstrating the effectiveness of our approach in capturing the underlying physics of AdS/QCD. In contrast with the GKK model [17], the dilaton profile we compute remains positive throughout the 5-dimensional space, which is consistent with the null energy condition [16, 39, 40]. The dilaton profile we obtain lies in-between the linear and quadratic functions. This finding is crucial because, though string theoretical models predict a linear dilaton profile, it would result in a continuum spectrum for the glueballs [41]. The dilaton wave profile, along with the scalar vevs, provides a deep enough potential for the pion wavefunction to support a ~ 135 MeV light state.

In Section 2, we briefly introduce the bottom-up AdS/QCD, including the scalar, pseudo-scalar, vector, axial-vector, and higher spin mesons. In Section 3, we discuss the methodology and define the Loss function for the neural network. Subsequently, in Section 4 we give the numerical results and predictions, and we conclude in Section 5.

2 Review of AdS/QCD

The AdS/QCD model is based on the idea that the strong coupling regime of QCD can be described by a classical gravitational theory in a higher-dimensional AdS space. The correspondence between the two theories allows us to study non-perturbative aspects of QCD using classical gravity calculations in AdS space. The fields in the AdS space correspond to operators in the gauge theory, and the dynamics of these fields can be used to compute correlation functions and other observables in the gauge theory.

The metric in the 5-D AdS space is given by,

$$g_{MN}dx^Mdx^N = e^{2A(z)} (dz^2 + \eta_{\mu\nu}dx^\mu dx^\nu), \quad (1)$$

where, z is defined as a dimensionless parameter related to the physical scale up to the radius of the AdS space (L) and the Minkowski metric is chosen to be $\eta_{\mu\nu} = \text{diag}(-1, +1, +1, +1)$.

The 5D action, in this geometry, with a bulk scalar field X transforming under the $SU(2)_L \times SU(2)_R$ symmetry is given by,

$$I = - \int d^5x \sqrt{-g} e^{-\phi(z)} \text{Tr} \left[|DX|^2 + m_X^2 |X|^2 - V(X) + \frac{1}{4g_5^2} (F_L^2 + F_R^2) \right], \quad (2)$$

where, $m_X^2 = -3$, $g_5^2 = 12\pi^2/N_c$ (N_c being the number of colors), $D^M X = \partial^M X - iA_L^M X + iXA_R^M$ is the covariant derivative, and $F_{L,R}^{MN} = \partial^M A_{L,R}^N - \partial^N A_{L,R}^M - i [A_{L,R}^M, A_{L,R}^N]$ are the field tensors. The scalar potential is taken to be $V(X) = \frac{4}{3}k_1 X^3 + 2k_2 X^4$ [12].

The scalar field X upon getting the VEV,

$$\langle X \rangle \equiv \frac{v(z)}{2} \begin{pmatrix} 1 & 0 \\ 0 & 1 \end{pmatrix}, \quad (3)$$

breaks the chiral symmetry $SU(2)_L \times SU(2)_R \rightarrow SU(2)_V$.

Varying the action, the dependence of VEV on the 5 dimensional space is given by,

$$\partial_z \left(e^{-\phi(z)+3A(z)} \partial_z v(z) \right) - e^{-\phi(z)+5A(z)} (m_X^2 v(z) - V_k(v)) = 0, \quad (4)$$

where, $V_k(v(z)) = \frac{\partial V(X)}{\partial X} \Big|_{X=v(z)} = k_1 v(z)^2 + k_2 v(z)^3$.

Demanding asymptotic AdS in the UV limit, the warp factor becomes $A(z)|_{z \rightarrow 0} = -\log(z)$ and the behavior of the VEV is given by,

$$v(z \rightarrow 0) = \alpha z + \beta z^3, \quad (5)$$

where,

$$\alpha = \zeta m_q L, \quad \beta = \frac{\Sigma}{\zeta} L^3. \quad (6)$$

Here, m_q is the quark mass, Σ is the chiral condensate, and $\zeta = \sqrt{N_c}/(2\pi)$ is a normalization factor [42]. The Gell-Mann-Oakes-Renner (GMOR) relation becomes,

$$f_\pi^2 m_\pi^2 = 2m_q \Sigma. \quad (7)$$

2.1 Meson Mass Spectrum

2.1.1 Scalar and Pseudo-Scalar Mesons

The fluctuations of the bulk scalar field X about the VEV could be written as $X(x, z) \equiv (v(z)/2 + S(x, z)) e^{2i\pi(x, z)}$, where $S(x, z)$ and $\pi(x, z)$ are the scalar and the pion fields respectively. And expanding the fluctuation S in its Kaluza-Klein modes (KK) $S(x, z) = \sum_n S_n(x) S_n(z)$, the equation of motion of S_n becomes,

$$\partial_z \left(e^{-B_2(z)} \partial_z S_n(z) \right) - e^{-B_2(z)} e^{2A(z)} (m_X^2 - (2k_1 v(z) + 3k_2 v^2(z))) S_n(z) = -e^{-B_2(z)} m_{S_n}^2 S_n(z), \quad (8)$$

where, $B_2(z) = \phi(z) - 3A(z)$, and m_{S_n} are the discrete eigenvalues of the Sturm-Liouville problem. These discrete values of $m_{S_n}^2$ correspond to the mass of the scalar mesons. This equation can be transformed into a Schrödinger equation, using the substitution $S_n(z) = e^{-B_2(z)/2} \psi_n(z)$, giving,

$$-\partial_z^2 \psi_n(z) + V_{f_0}(z) \psi_n(z) = m_{S_n}^2 \psi_n(z), \quad (9)$$

with the effective potential $V_{f_0}(z)$ given by,

$$V_{f_0} = \left[\frac{1}{4} (\partial_z B_2)^2 - \frac{1}{2} \partial_z^2 B_2 + e^{2A(z)} (m_X^2 - (2k_1 v(z) + 3k_2 v^2(z))) \right]. \quad (10)$$

Upon investigating the UV behavior of the potential V_{f_0} , we observe that $V_{f_0}(z \rightarrow 0) \rightarrow +\infty$, which ensures that the wave-function $\psi_n(z)$ goes to zero at the UV boundary, along with the normalizability condition $\psi_n(z \rightarrow \infty) \rightarrow 0$.

Varying the action with respect to the pion field $\pi(x, z)$, and expanding it in its KK modes, $\pi(x, z) = \sum_n \Pi_n(x) \pi_n(z)$, the equation of motion becomes,

$$\frac{e^{B_2(z)}}{v^2(z)} \partial_z \left(v^2(z) e^{-B_2(z)} \partial_z \pi_n \right) + m_{\pi n}^2 (\pi_n - \xi_n) = 0, \quad (11)$$

here, we work in the gauge $A_5 = 0$. The longitudinal component of the axial vector field, $A_\mu = (A_{L\mu} - A_{R\mu})/2$, is denoted by $\xi(x, z) = \sum_n \Xi_n(x) \xi_n(z)$, where n denotes the KK mode.

Also, varying the action with respect to the longitudinal component of the axial vector field, $\xi_n(z)$, gives the equation of motion,

$$\partial_z \left(e^{-B_1(z)} \partial_z \xi_n \right) + g_5^2 v^2(z) e^{-B_2(z)} (\pi_n - \xi_n) = 0, \quad (12)$$

where $B_1(z) = \phi(z) - A(z)$. To solve these coupled differential equations, it is possible to combine Eq.11 and Eq.12, into a Schrödinger-like equation [19], but doing so eliminates information from the mass spectrum [43,44]. Specifically, we will only be able to get the mass eigenvalues corresponding to the excited states, and lose information of the ground state mass. We therefore choose to solve these two coupled second-order differential equations directly. Simplifying these equations, we get,

$$\begin{aligned} \partial_z^2 \pi_n + \omega(z) \partial_z \pi_n + m_{\pi n}^2 (\pi_n - \xi_n) &= 0, \\ \partial_z^2 \xi_n - (\partial_z B_1(z)) \partial_z \xi_n + C(z) (\pi_n - \xi_n) &= 0, \end{aligned} \quad (13)$$

where $\omega(z) = 2\partial_z v(z)/v(z) - \partial_z B_2(z)$ and $C(z) = g_5^2 v^2(z) e^{2A(z)}$. These two equations can be solved with the boundary conditions $\pi_n = 0$ and $\xi_n = 0$ at $z \rightarrow 0$ and $z \rightarrow \infty$ to obtain the mass spectrum of the pseudo-scalar mesons.

2.1.2 Vector and Axial-Vector Mesons

For the vector mesons, $V_\mu = (A_{L\mu} + A_{R\mu})/2$, fixing the gauge $V_5 = 0$, the transverse component of the vector field can be expanded in terms of its KK modes as $V_{\mu\perp}^n(x, z) = \sum_n \mathcal{V}_\mu^{(n)}(x) V_n(z)$. Now, the equation of motion of $V_n(z)$ becomes,

$$-\partial_z \left(e^{-B_1(z)} \partial_z V_n(z) \right) + m_{Vn}^2 e^{-B_1(z)} V_n(z) = 0, \quad (14)$$

where $B_1(z) = \phi(z) - A(z)$, and m_{Vn}^2 are the mass eigenvalues corresponding to the masses of the vector meson. To bring this equation to a Schrödinger-like form we substitute, $V_n(z) = e^{B_1(z)/2} \psi_{Vn}(z)$ and obtain,

$$-\partial_z^2 \psi_{Vn}(z) + V_\rho \psi_{Vn}(z) = m_{Vn}^2 \psi_{Vn}(z), \quad (15)$$

where the effective potential is given by,

$$V_\rho = \left[\frac{1}{4} (\partial_z B_1)^2 - \frac{1}{2} \partial_z^2 B_1 \right]. \quad (16)$$

The mass of the vector mesons are computed by demanding Dirichlet boundary condition for ψ_{Vn} at UV and for large z .

Similarly, for the axial-vector mesons, choosing the gauge $A_5 = 0$, and expanding the axial vector field in its KK decomposition, $A_{\mu\perp}^n(x, z) = \mathcal{A}_\mu^{(n)}(x)a_n(z)$, we get the equation of motion for $a_n(z)$ as,

$$\partial_z(e^{-B_1(z)}\partial_z a_n) + \left(m_{an}^2 - g_5^2 e^{2A(z)}v^2(z)\right)e^{-B_1(z)}a_n = 0. \quad (17)$$

Here we denote the axial-vector meson masses by m_{an}^2 . Substituting $a_n(z) = e^{B_1(z)/2}\psi_{An}(z)$, we obtain,

$$-\partial_z^2\psi_{An}(z) + V_{a_1}\psi_{An}(z) = m_{An}^2\psi_{An}(z), \quad (18)$$

such that $\psi_{An}(z)$ satisfies Dirichlet boundary condition at UV and at large z . The effective potential is given by,

$$V_{a_1} = \left[\frac{1}{4}(\partial_z B_1)^2 - \frac{1}{2}\partial_z^2 B_1 + g_5^2 e^{2A(z)}v^2(z)\right]. \quad (19)$$

2.1.3 Higher-Spin Mesons

To study the higher spin mesons, consider a rank- G symmetric tensor field, and following the same procedure as before, we can show that the z -dependent part of the 5-D bulk tensor field ($G(x, z) = \sum_n \mathcal{G}_n(x)G_n(z)$) follows the equation of motion,

$$-\partial_z\left(e^{-B_G(z)}\partial_z G_n(z)\right) + m_{Gn}^2 e^{-B_G(z)}G_n(z) = 0, \quad (20)$$

where $B_G(z) = \phi(z) - (2G - 1)A(z)$. For a spin-2 meson like the a_2 meson, we have $G = 2$ and substituting $G_n(z) = e^{B_G(z)/2}\psi_{Gn}(z)$, we obtain the Schrödinger-like equation,

$$-\partial_z^2\psi_{Gn}(z) + V_{a_2}\psi_{Gn}(z) = m_{Gn}^2\psi_{Gn}(z), \quad (21)$$

where the effective potential is given by,

$$V_{a_2} = \left[\frac{1}{4}(\partial_z B_2)^2 - \frac{1}{2}\partial_z^2 B_2\right]. \quad (22)$$

with $B_2(z) = \phi(z) - 3A(z)$. The mass eigenvalues m_{Gn}^2 of the spin-2 meson are obtained again by solving the equation of motion and imposing the Dirichlet boundary conditions on the wave functions.

With these, in the next section we discuss a neural network architecture to solve the Schrödinger-like equations, along with the boundary conditions, to obtain the warp factor, dilaton profile, and the chiral symmetry breaking potential by training the model with the masses m_{Sn} , m_{Vn} , m_{An} and m_{Gn} in Table 1. Moreover, the network will predicted the mass spectrum of pions $m_{\pi n}$ and match with the experimental values.

3 Methodology

3.1 Model Architecture

We model the warp factor $A(z)$ and the scalar VEV $v(z)$ using a trainable neural network. We take two feed-forward neural networks with input $z \in (0, z_{max})$, and outputs a scalar value $A_{NN}(z)$ and $v_{NN}(z)$ respectively. The value of z_{max} is chosen sufficiently large such that boundary conditions on

wavefunctions are satisfied. We employ a transformation function on the output of the neural network to get the approximated functions for the warp factor $A(z)$ and $v(z)$, defined as

$$\begin{aligned} A(z) &= -\ln(z) + zA_{\text{NN}}(z) , \\ v(z) &= \frac{\alpha z + \beta z^3 + v_{\text{NN}}(z)z^4}{1+z^3} , \end{aligned} \quad (23)$$

This transformation ensures the correct boundary condition at the UV region. The denominator in $v(z)$ is introduced in order to prevent numerical instability in the IR region.

While training, the chiral condensate (Σ) is made sure to lie within a reasonable range ($0.01 \text{ GeV}^3 : 0.03 \text{ GeV}^3$), and is defined in terms of the training parameter θ as,

$$\Sigma = a + (b - a)\sigma(\theta) \quad (24)$$

where, σ is the sigmoid function and $a = 0.01 \text{ GeV}^3$ and $b = 0.03 \text{ GeV}^3$. The quark mass m_q is then computed using the GMOR relation given in Eq. 7 and this is, in turn, used to compute the α and β values from Eq. 6.

For a background $A(z)$ and the VEV $v(z)$ trained with Eq. 23, the $B_2(z)$ could be computed from Eq. 4 as,

$$\partial_z B_2(z) = \frac{1}{\partial_z v(z)} \left(\partial_z^2 v(z) + e^{2A(z)} (3v(z) + V_k(v(z))) \right), \quad (25)$$

where, $m_X^2 = -3$ and,

$$V_k(v(z)) = k_1 v(z)^2 + k_2 v(z)^3. \quad (26)$$

The coefficients k_1 and k_2 are the trainable parameters. Although we trained the model using only the quartic interaction term, it was found that adding a cubic interaction term significantly reduced the loss. This may indicate either insufficient hyperparameter tuning in the quartic-only case or that a cubic interaction is genuinely required in the holographic model.

With $\partial_z B_2(z)$ computed in Eq. 25, we obtain,

$$\partial_z B_1(z) = \partial_z B_2(z) + 2 \partial_z A(z), \quad \partial_z \phi(z) = \partial_z B_2(z) + 3 \partial_z A(z). \quad (27)$$

Using these relations, the effective potentials appearing in Eq. 10, Eq. 16, Eq. 19, and Eq. 22 are evaluated. The resulting Schrödinger-like equations are then solved numerically using the finite-difference method, with boundary conditions $\psi_n(0) = 0$ and $\psi_n(z_{\text{max}}) = 0$, yielding the meson mass eigenvalues.

The AdS radius L is determined in terms of the trainable parameter l as,

$$L = \log(1 + l^2), \quad (28)$$

to ensures that it remains positive while also preventing it from taking excessively large values, while training.

The values of k_1 and k_2 significantly influence the potentials and, consequently, the mass spectrum. Choosing a good initial guess for these parameters is crucial for the convergence of the training. The initial values of the trainable parameters k_1 and k_2 are chosen using a Bayesian optimization algorithm called the Tree-Structured Parzen Estimator (TPE) [45] from the Optuna library [46] (See Appendix B for more details). The initial values of the other two trainable parameters are taken as $\theta = 0.0$ and $l = 1.0$. With the two neural network for $A(z)$ and $v(z)$, and the four trainable parameters θ , k_1 , k_2 , and l , we aim to fit the meson mass spectra scalar (f_0), vector (ρ), axial-vector (a_1) and spin-2 (a_2) mesons,

and use the trained model to predict the masses of the pseudo-scalar (π) mesons by solving Eq. 13. The mass eigenvalues are calculated using the finite-difference method by writing the discretized form of the Schrödinger-like equations in matrix form. This discretized form is constructed by discretizing the z -coordinate (See Appendix A). The mass eigenvalues of the Schrödinger-like equations are directly controlled by the value of the effective potential at these discretized points, which appear as the diagonal elements of the matrix. Therefore, the model trains the values of the functions $A(z)$ and $v(z)$ at these discretized points, thereby learning the effective potential which can yield the correct mass eigenvalue.

3.2 Loss Functions

To get the mass eigenvalues, we solve the Schrödinger-like equations using the finite-difference method. We discretize the spatial coordinate z into N points ranging from $z = 0$ to $z = z_{max}$ with a step size of h . The discretized form of the Schrödinger-like equation $-\partial_z^2\psi(z) + V_\mu(z)\psi(z) = \lambda_\mu\psi(z)$ can be written in the form of a matrix eigenvalue problem (See Appendix A), which can be solved using numerical eigenvalue solvers to obtain the non-dimensional mass eigenvalues λ_μ for the meson type $\mu \in \{\rho, a_1, a_2, f_0\}$. The Dirichlet boundary conditions $\psi(0) = 0$ and $\psi(z_{max}) = 0$ result in a real symmetric tri-diagonal matrix whose eigenvalues can be efficiently computed using the `torch.linalg.eigvalsh` function in PyTorch, which under the hood uses the LAPACK library (or its GPU analogs). It returns the eigenvalues in ascending order. To convert them to physical units, the eigenvalues are divided by L^2 ,

$$m_{\mu,n}^2 = \frac{\lambda_{\mu,n}}{L^2} \quad (29)$$

where, L is the AdS radius and μ index identifies the meson type (scalar f_0 , axial vector a_1 , vector ρ or tensor a_2). The error for the n^{th} mass of the meson is given by,

$$E_{\mu,n} = \frac{|m_{\mu,n}^2 - \omega_{\mu,n}^2|}{\omega_{\mu,n}^2}, \quad (30)$$

where ω_n are the experimental values of the meson masses as given in [47]. The Loss function now becomes,

$$\mathcal{L}_{\text{mass}}^{(\mu)} = \frac{1}{N_\mu} \sum_{n=1}^{N_\mu} \Lambda_{\mu,n} E_{\mu,n}, \quad (31)$$

where N_μ is the number of excited mesons considered for each kind, and $\Lambda_{\mu,n}$ is a hyperparameter that controls the weightage of each meson mass in the total loss function. We have employed an adaptive weighting scheme where $\Lambda_{\mu,n}$ at each training step is proportional to the loss contributed by that particular mass (See Appendix B: Eq. 49). This ensures that the model focuses more on the masses that are harder to fit. The total mass loss function used in the training is given by

$$\mathcal{L}_{\text{mass}} = \mathcal{L}_{\text{mass}}^{(\rho)} + \mathcal{L}_{\text{mass}}^{(a_1)} + \mathcal{L}_{\text{mass}}^{(a_2)} + \mathcal{L}_{\text{mass}}^{(f_0)}. \quad (32)$$

It is essential for the Loss function to be differentiable so that the gradients can be calculated using backpropagation. Although the internal algorithm (LAPACK) itself is not automatically differentiable, the PyTorch library has implemented a mathematical formula that is pre-programmed into it. (See Appendix A for more details.)

The equation for $\partial_z B_2$ given in Eq. 25 can become numerically unstable if $\partial_z v(z) = 0$. Since $\partial_z v(z)|_{z=0} = \alpha$, and α is positive, we demand that $\partial_z v(z) > 0$ for all z . This ensures that $\partial_z v(z)$ never

crosses zero, therefore avoiding numerical instabilities. To enforce this condition, we add another penalty term to the loss function given by

$$\mathcal{L}_{v'} = \text{ReLU}(-\partial_z v(z)), \quad (33)$$

where ReLU is the rectified linear unit function defined as $\text{ReLU}(x) = \max(0, x)$. This term penalizes any negative values of $\partial_z v(z)$.

To confine the wavefunction within the AdS space and ensure normalizability of the wavefunction at large z , we expect the potentials $V_\mu(z)$ to be non-decreasing functions of z in the IR region. This can be imposed by demanding that $\partial_z V_\rho(z)$ and $\partial_z V_{a_2}(z)$ are positive at large z . This automatically also ensures that the potentials given in Eq. 10 and Eq. 19 and are also confining. To impose this condition, we add another penalty term to the loss function given by

$$\mathcal{L}_{\text{pot}} = \text{ReLU}(-\partial_z V_\rho(z)) + \text{ReLU}(-\partial_z V_{a_2}(z)), \quad (34)$$

where z is chosen randomly at each training step at a sufficiently large value close to z_{max} . We expect $A(z)$ to be negative and decreasing at the IR from warped geometry. This is imposed by adding another penalty term,

$$\mathcal{L}_A = \text{ReLU}(A(z_{\text{max}}) + \ln(z_{\text{max}}) - \Delta), \quad (35)$$

where Δ is a constant. The total loss function now becomes,

$$\mathcal{L}_{\text{tot}} = \mathcal{L}_{\text{mass}} + \Lambda_{v'} \mathcal{L}_{v'} + \Lambda_{\text{pot}} \mathcal{L}_{\text{pot}} + \Lambda_A \mathcal{L}_A, \quad (36)$$

where $\Lambda_{v'}$, Λ_{pot} , and Λ_A are hyperparameters that control the weightage of the penalty terms. The model is trained to minimize the total loss function \mathcal{L}_{tot} by optimizing the neural network's weights and biases, as well as the trainable parameters θ , k_1 , k , and L .

4 Numerical Results

We perform a hyperparameter search for the initial values of k_1 and k_2 using Optuna's built-in TPE sampler, in the range $[-15, 15]$ (See Appendix B). We observe that the model converges to a lower loss value for negative k_1 and positive k_2 , resulting in a bounded scalar field potential. The best initial guess was found to be around $k_1 = -7.4$ and $k_2 = 12.2$. With this initial guess, we train our model several times and select only those runs in which the total loss converges to a value below 0.01. We have selected 10 such runs, whose training loss and the trained model parameters (k_1, k_2, L, θ) corresponding to each run are listed in Table 5. Further details of the training procedure, along with the hyperparameters used, are provided in Appendix B.

L	$1.7051 \pm 0.2638 \text{ GeV}^{-1}$	θ	2.4094 ± 1.3162
k_1	-7.7745 ± 1.0499	k_2	17.0736 ± 2.7509

Table 2: The trained model parameters $L = \log(1 + l^2)$, θ , k_1 and k_2 . The values are given as mean \pm standard deviation over different runs.

The trained functions $v(z)$ and $A(z)$ are shown in Fig. 1, and the mean of the model parameters obtained over different runs is given in Table 2. The trained parameter θ can be used to get the value of Σ from Eq. 24, and use the GMOR relation in Eq. 7 to get m_q as,

$$\Sigma = (0.3004 \pm 0.0127 \text{ GeV})^3 \quad \text{and} \quad m_q = 0.0031 \pm 0.0005 \text{ GeV}, \quad (37)$$

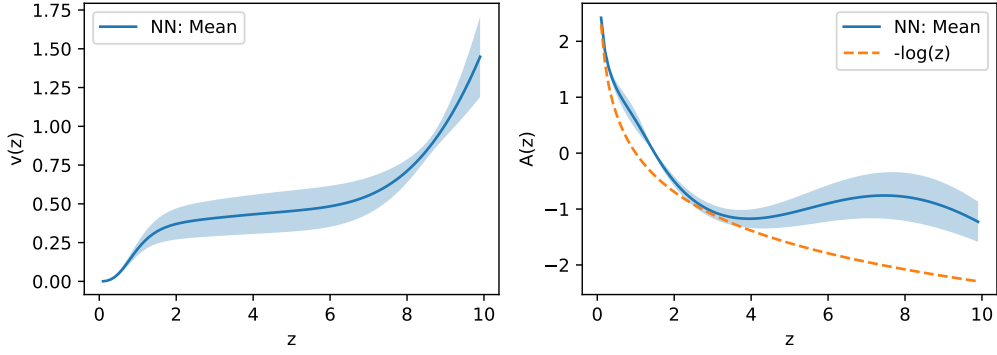


Figure 1: The learned functions $v(z)$ (left) and $A(z)$ (right) after training. The shaded regions represent the standard deviation over different runs, and the solid lines represent the mean value.

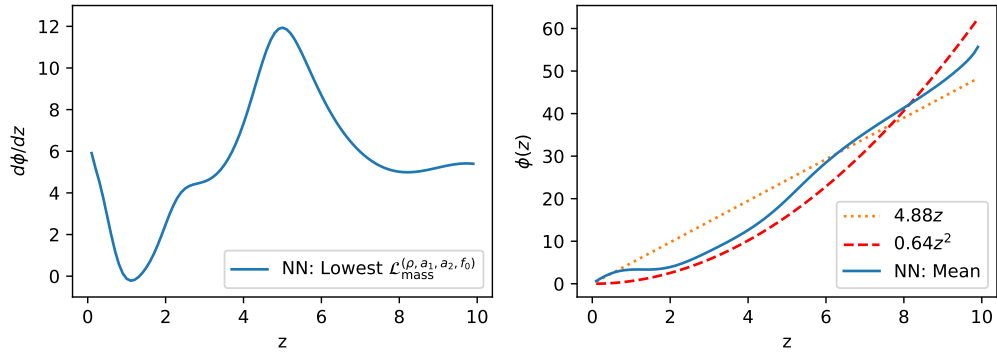


Figure 2: The plot of $d\phi/dz$ (left) and $\phi(z)$ (right). The solid line represents the best fit corresponding to the minimum value of $\mathcal{L}_{\text{mass}}^{(\rho, a_1, a_2, f_0)}$. Unlike Figs. 1 and 2, where the spread was symmetric and shown as mean \pm standard deviation, the $d\phi/dz$ here exhibit a skewed variation, which is why we only plot the $d\phi/dz$ corresponding to the best run. However, the $\phi(z)$ (right panel) obtained shows a symmetric spread, which is represented by the mean. The dotted line and the dashed line in the right panel represent a linear and quadratic fit to the mean value of $\phi(z)$, respectively.

where the values are given as mean \pm standard deviation over different runs. With the given $v(z)$ and $A(z)$, we can obtain $d\phi/dz$ which is plotted in Fig. 2 (left). We observe a large variation in $d\phi/dz$ across different runs, especially in the IR region. Integrating $d\phi/dz$ gives us $\phi(z)$ up to an additive constant, also given in Fig. 2 (right). The $\phi(z)$, unlike $d\phi/dz$, shows a much more symmetric spread across different runs. We have plotted a linear and quadratic fit to the mean value of $\phi(z)$. Additionally, we plot the effective potentials for the ρ , a_1 , a_2 , and f_0 mesons in Fig. 3. Like the $d\phi/dz$, these potentials also exhibit a broader and more skewed variation across different runs.

The predicted spectra of the trained masses of the ρ , a_1 , a_2 , and f_0 mesons obtained from our model are given in Table 3 and are plotted with respect to n (radial excitation number) in Fig. 4. The predicted masses show good agreement with the experimental values, with a maximum error of around 4.23%.

To test our model, we predict the masses of the pseudo-scalar meson π . We use the finite difference method to solve the coupled second-order differential equation given in Eq. 13 using the learned

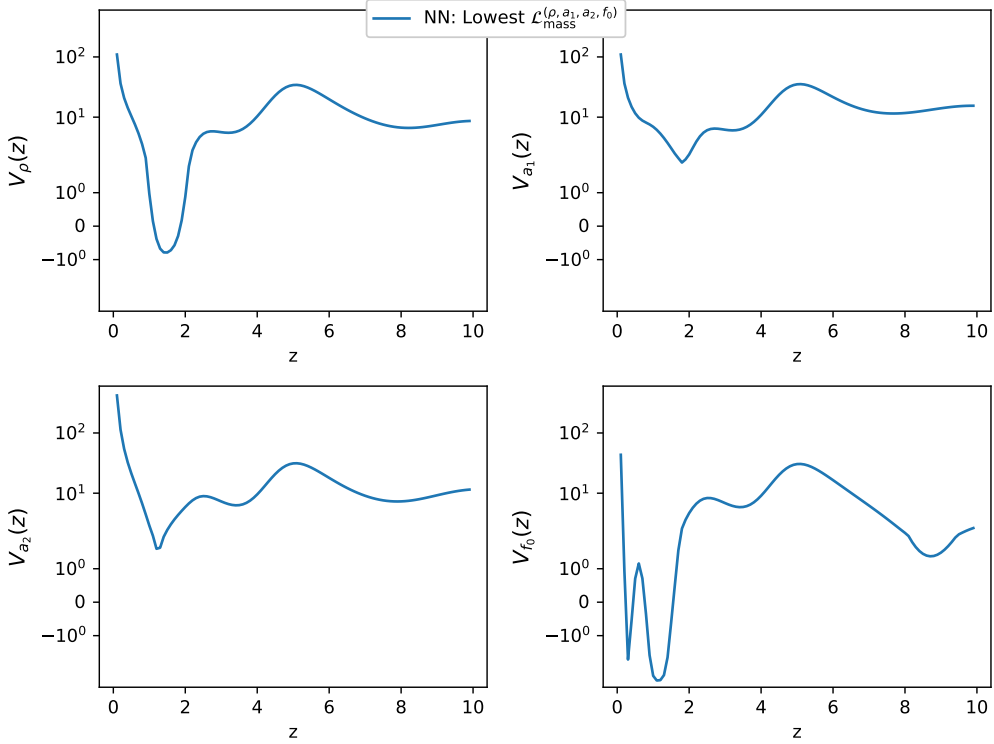


Figure 3: Effective potentials for the ρ , a_1 , a_2 , and f_0 mesons. The solid line represents the best fit corresponding to the minimum value of $\mathcal{L}_{\text{mass}}^{(\rho, a_1, a_2, f_0)}$.

parameters and functions. This time, we obtain a matrix for a generalized eigenvalue equation (see Appendix A for more details), which we solve using SciPy’s built-in function `scipy.linalg.eigvals`.

The predicted masses eigenvalues m_n obtained (after converting to physical units) using our trained model are given in Table 4 and plotted in Fig. 5. Here, the best fit values are obtained for the run with the lowest value of $\mathcal{L}_{\text{mass}}^{(\pi)}$. The Loss corresponding to the π meson masses for each run is given in Table 5. Although we have not trained our model to fit the π meson masses, the predicted values match the experimental data fairly well, except for the first excited state, where the model has overshoot the mass by a large amount.

5 Conclusion

The bottom-up approach in holographic QCD explores the functional space of all possible background metrics and scalar potentials, searching for functions that best fit the QCD observables. With enough phenomenological and theoretical constraints, the bottom-up approach can severely restrict the allowed background functions and may select a class of viable models, though not necessarily a unique one. We have provided a deep-learning architecture that searches in the possible functional space of the warp-factor $A(z)$, the dilaton profile $\phi(x)$, along with the possible values of cubic (k_1) and quartic (k_2) terms in the scalar potential, and the quark condensate Σ . This space is constrained by fitting the mass spectrum of the unflavored mesons (ρ , a_1 , a_2 and f_0) and their excitations.

Meson	State	Predicted Mass (GeV)	% Error
ρ	1	0.79 ± 0.01	2.93%
	2	1.46 ± 0.01	0.83%
	3	1.61 ± 0.01	2.84%
	4	1.77 ± 0.02	4.23%
	5	1.91 ± 0.03	0.70%
	6	2.11 ± 0.02	1.91%
a_1	1	1.25 ± 0.01	1.06%
	2	1.64 ± 0.01	0.25%
a_2	1	1.31 ± 0.01	0.46%
	2	1.66 ± 0.01	2.20%
f_0	1	0.49 ± 0.00	1.36%
	2	0.98 ± 0.01	0.02%
	3	1.39 ± 0.03	1.75%
	4	1.50 ± 0.04	0.20%
	5	1.67 ± 0.02	1.96%
	6	1.83 ± 0.02	0.12%
	7	1.98 ± 0.03	1.24%
	8	2.13 ± 0.02	0.97%
	9	2.28 ± 0.02	1.01%
	10	2.42 ± 0.03	0.88%

Table 3: Predicted meson masses (in GeV). The predictions are reported as the mean \pm standard deviation across different runs. The % Error is calculated with respect to the mean value of the predicted mass.

State	Predicted Mass (GeV)	Experimental Mass (GeV)	Best Fit: Lowest $\mathcal{L}_{\text{mass}}^{(\pi)}$ (GeV)	% Error
1	0.161 ± 0.057	0.135	0.127	5.36
2	1.681 ± 0.021	1.3 ± 0.1	1.664	28.02
3	1.833 ± 0.049	1.8 ± 0.009	1.854	2.99

Table 4: Predicted and Experimental π meson masses (in GeV) [47]. The predicted masses are reported as the mean \pm standard deviation across different runs. The best fit values correspond to the run with lowest $\mathcal{L}_{\text{mass}}^{(\pi)}$ in Table 5. The percentage error is computed with respect to the best-fit value.

The duality between AdS/QCD and deep neural networks, as shown in [48], raises intriguing questions about their physical origins and suggests a new methodology for investigating both frameworks. This was pioneered in [27], where the authors trained for the masses of the ρ and a_1 meson, through which the $A(z)$ and $\phi(z)$ were determined. They solved the differential equation of the KK mode using the Euler method, which, unfortunately, results in the accumulation of local truncation error at each iteration. The eigenvalues are calculated by traversing all the values of masses to search for the mass for which KK modes are normalizable. Since the axial sector was not studied, the information about the chiral symmetry breaking by the bulk scalar field is not well understood. Including the higher meson masses and axial sector, along with the f_0 mesons, becomes computationally challenging because the network's structure is determined by the theory itself.

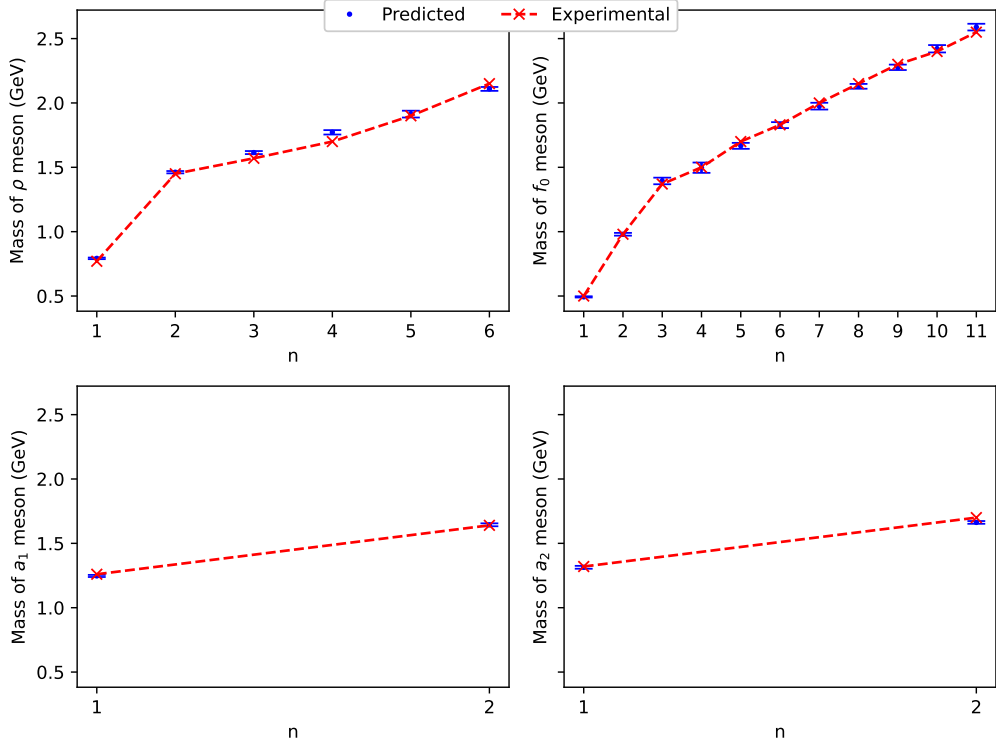


Figure 4: Mass spectra of the ρ , f_0 , a_1 and a_2 mesons [47]. The predicted masses correspond to the mean, and the error bars show the standard deviation across multiple runs.

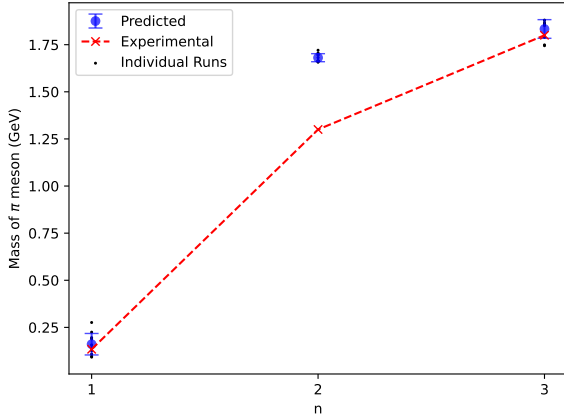


Figure 5: Mass spectrum of the predicted π meson as shown in Table 4. The error bars represent the standard deviation over different runs.

In contrast, we propose here to train the architecture using the finite difference method to directly obtain the mass eigenvalue, making it more efficient, less error-prone, and more extensible to higher excitation states of the meson tower. Additionally, the introduction of the scalar vev has enabled us to determine the masses of all unflavored mesons. This strategy is flexible and highly tunable, which leaves scope for employing additional constraints on the functional space in the form of additional loss functions.

The strategy we use here is described in Appendix A, where the eigenvalues and functions of the Schrödinger-like equations are computed by diagonalizing the matrix obtained from latticized 5-dimensional space. Unlike in [27], here there is no emergent metric arising from the AdS/DL correspondence; instead, the framework closely follows the latticized 5D action via dimensional deconstruction [30–38] to obtain a linear moose model. The neural network enters the linear moose model at the prediction of the potential for the wavefunction.

Though the z^2 behavior for the dilaton profile is anticipated by several phenomenological models [12, 17, 18, 23] for linear confinement, string theoretic models often assume a linear profile. In this work, the predicted dilaton, in Fig.2, exhibits a profile in between the linear and quadratic types, which is positive throughout the region, making it consistent with the null energy condition [39]. Moreover, it predicted the pion mass and its excitations with good accuracy. As mentioned earlier, our numerical experiment suggests that for a more precise fitting of the mass spectra, a cubic interaction, in addition to the quartic interaction, is necessary.

Acknowledgments

M.T.A. acknowledges the financial support of DST through the INSPIRE Faculty grant DST/INSPIRE/04/2019/002507.

Appendix

A Numerical Routine

The discretized form of the Schrödinger-like equations $-\partial_z^2\psi(z) + V_\mu(z)\psi(z) = \lambda_\mu\psi(z)$ for $\mu \in \{\rho, a_1, a_2, f_0\}$ is given by

$$-\frac{\psi(z+h) - 2\psi(z) + \psi(z-h)}{(h)^2} + V_\mu(z)\psi(z) = \lambda_\mu\psi(z), \quad (38)$$

where λ_μ is the eigenvalue of the equation and h is the step size. This can be written in the matrix form as

$$\frac{1}{h^2} \begin{pmatrix} 2 + h^2V_\mu(z_1) & -1 & 0 & \cdots & 0 \\ -1 & 2 + h^2V_\mu(z_2) & -1 & \cdots & 0 \\ 0 & -1 & 2 + h^2V_\mu(z_3) & \cdots & 0 \\ \vdots & \vdots & \vdots & \ddots & \vdots \\ 0 & 0 & 0 & \cdots & 2 + h^2V_\mu(z_{N-1}) \end{pmatrix} \begin{pmatrix} \psi(z_1) \\ \psi(z_2) \\ \psi(z_3) \\ \vdots \\ \psi(z_{N-1}) \end{pmatrix} = \lambda_\mu \begin{pmatrix} \psi(z_1) \\ \psi(z_2) \\ \psi(z_3) \\ \vdots \\ \psi(z_{N-1}) \end{pmatrix}$$

where $z_i = z_0 + ih$ for $i = 0, 1, 2, \dots, N$, and we have taken the boundary conditions $\psi(z_0) = \psi(z_N) = 0$, since we expect the wavefunction to vanish at the boundaries $z = 0$ and $z = z_{max}$. To get the non-dimensional mass eigenvalues λ_μ , we solve for the eigenvalue of the matrix H_μ given by

$$H_\mu = \frac{1}{h^2} \begin{pmatrix} 2 + h^2V_\mu(z_1) & -1 & 0 & \cdots & 0 \\ -1 & 2 + h^2V_\mu(z_2) & -1 & \cdots & 0 \\ 0 & -1 & 2 + h^2V_\mu(z_3) & \cdots & 0 \\ \vdots & \vdots & \vdots & \ddots & \vdots \\ 0 & 0 & 0 & \cdots & 2 + h^2V_\mu(z_{N-1}) \end{pmatrix} \quad (39)$$

We use PyTorch's built-in function `torch.linalg.eigvalsh` to compute the eigenvalues of this real symmetric tridiagonal matrix, which returns the eigenvalues in ascending order. Under the hood, PyTorch utilizes the LAPACK library (or its GPU counterparts) to efficiently compute eigenvalues. Since the LAPACK algorithm used is not automatically differentiable, PyTorch's `torch.linalg.eigvalsh` uses a pre-programmed mathematical formula to compute the gradients of the eigenvalues with respect to the elements of the matrix. We derive a basic formula to calculate derivatives of eigenvalues of a real symmetric matrix [20].

Considering $A \in \mathbb{R}^{n \times n}$ to be a real symmetric matrix,

$$\begin{aligned} A &= Q\Lambda Q^T, \\ \Rightarrow AQ &= Q\Lambda, \end{aligned} \tag{40}$$

where $Q \in \mathbb{R}^{n \times n}$ is an orthogonal matrix ($Q^T Q = I$) and $\Lambda = \text{diag}(\lambda_1, \lambda_2, \dots, \lambda_n)$. Differentiating both sides and multiplying by Q^T from the left, we get

$$Q^T(dA)Q + Q^T A(dQ) = Q^T(dQ)\Lambda + (d\Lambda).$$

We define $\Omega = Q^T(dQ)$, which is a skew-symmetric matrix (since $Q^T Q = I \Rightarrow Q^T(dQ) + (dQ)^T Q = 0 \Rightarrow \Omega^T = -\Omega$). Substituting this in the above equation, we get

$$Q^T(dA)Q + \Lambda\Omega = \Omega\Lambda + d\Lambda,$$

whose diagonal part is

$$d\lambda_i = q_i^T(dA)q_i,$$

where q_i is the normalized eigenvector corresponding to the eigenvalue λ_i (since each column of Q is a normalized eigenvector of A). Using this, we can calculate the derivative of the eigenvalue with respect to any parameter w as

$$\frac{d\lambda_i}{dw} = q_i^T \left(\frac{dA}{dw} \right) q_i. \tag{41}$$

This equation is the celebrated Hellmann-Feynman theorem [49] in quantum mechanics that relates the derivative of an eigenvalue of a Hamiltonian to the expectation value of the derivative of the Hamiltonian operator. PyTorch cleverly uses the eigenvectors q_i to efficiently compute the gradients during the backward pass.

To get the mass eigenvalues of the pseudo-scalar meson π , we need to solve the coupled second-order differential equation given in Eq. 13. The discretized form of the coupled equation is given by

$$\begin{aligned} \frac{\pi_{i+1} - 2\pi_i + \pi_{i-1}}{h^2} + \omega(x_i) \frac{\pi_{i+1} - \pi_{i-1}}{2h} &= m_n^2(-\pi_i + \xi_i) \\ C(z_i)\pi_i + \frac{\xi_{i+1} - 2\xi_i + \xi_{i-1}}{h^2} - B'_1(z_i) \frac{\xi_{i+1} - \xi_{i-1}}{2h} - C(z_i)\xi_i &= 0, \end{aligned} \tag{42}$$

where $B'_1(z) = \partial_z B_1(z)$, $\pi_i = \pi(z_i)$ and $\xi_i = \xi(z_i)$. For the boundary condition, $\pi_0 = \pi_N = 0$ and $\xi_0 = \xi_N = 0$, we can write this equation in terms of a matrix as

$$M\boldsymbol{\Psi} = m_n^2 T \boldsymbol{\Psi}, \tag{43}$$

where $\boldsymbol{\Psi} = (\pi_1, \pi_2, \dots, \pi_{N-1}, \xi_1, \xi_2, \dots, \xi_{N-1})^T$, and the matrices M and T can be written with block matrices as

$$M = \begin{pmatrix} M_1 & 0 \\ M_2 & M_3 \end{pmatrix}, \quad T = \begin{pmatrix} -\mathbb{I} & \mathbb{I} \\ 0 & 0 \end{pmatrix}, \tag{44}$$

where \mathbb{I} is the identity matrix of size $(N-1) \times (N-1)$, and the M_1 , M_2 and M_3 are $(N-1) \times (N-1)$ block matrices given by,

$$M_1 = \begin{pmatrix} \frac{-2}{h^2} & \left(\frac{1}{h^2} + \frac{\omega(z_1)}{2h}\right) & 0 & \cdots & 0 \\ \left(\frac{1}{h^2} - \frac{\omega(z_2)}{2h}\right) & \frac{-2}{h^2} & \left(\frac{1}{h^2} + \frac{\omega(z_2)}{2h}\right) & \cdots & 0 \\ 0 & \left(\frac{1}{h^2} - \frac{\omega(z_3)}{2h}\right) & \frac{-2}{h^2} & \cdots & 0 \\ \vdots & \vdots & \vdots & \ddots & \vdots \\ 0 & 0 & 0 & \cdots & \frac{-2}{h^2} \end{pmatrix}, \quad (45)$$

$$M_2 = \begin{pmatrix} C(z_1) & 0 & \cdots & 0 \\ 0 & C(z_2) & \cdots & 0 \\ \vdots & \vdots & \ddots & \vdots \\ 0 & 0 & \cdots & C(z_{N-1}) \end{pmatrix}, \quad (46)$$

$$M_3 = \begin{pmatrix} \left(\frac{-2}{h^2} - C(z_1)\right) & \left(\frac{1}{h^2} - \frac{B'_1(z_1)}{2h}\right) & 0 & \cdots & 0 \\ \left(\frac{1}{h^2} + \frac{B'_1(z_2)}{2h}\right) & \left(\frac{-2}{h^2} - C(z_2)\right) & \left(\frac{1}{h^2} - \frac{B'_1(z_2)}{2h}\right) & \cdots & 0 \\ 0 & \left(\frac{1}{h^2} + \frac{B'_1(z_3)}{2h}\right) & \left(\frac{-2}{h^2} - C(z_3)\right) & \cdots & 0 \\ \vdots & \vdots & \vdots & \ddots & \vdots \\ 0 & 0 & 0 & \cdots & \left(\frac{-2}{h^2} - C(z_{N-1})\right) \end{pmatrix} \quad (47)$$

We solve the generalized eigenvalue equation given in Eq. 43 using `scipy.linalg.eigvals` giving us the non-dimensional mass eigenvalues m_n^2 . The eigenvalues obtained are sorted in ascending order, and the first few eigenvalues are taken as the mass spectrum of the pseudo-scalar mesons.

It is possible to convert the generalized eigenvalue equation in Eq. 43 to a standard eigenvalue equation by decoupling the equations

$$M_1 \boldsymbol{\pi} = m_n^2 \mathbb{I}(-\boldsymbol{\pi} + \boldsymbol{\xi}) \quad \text{and} \quad M_2 \boldsymbol{\pi} + M_3 \boldsymbol{\xi} = 0 \quad (48)$$

where $\boldsymbol{\pi} = (\pi_1, \pi_2, \dots, \pi_{N-1})^T$ and $\boldsymbol{\xi} = (\xi_1, \xi_2, \dots, \xi_{N-1})^T$. We can use the second equation to express either $\boldsymbol{\pi}$ or $\boldsymbol{\xi}$ in terms of the other variable, and substituting it in the first equation gives us a standard eigenvalue equation. However, this involves calculating the inverse of several matrices, which can inculcate numerical errors. We have also observed that using this method leads to degeneracies in the eigenvalues, which are not observed when solving the generalized eigenvalue equation directly. Additionally, information about the eigenvectors is also lost in this process. Hence, we choose to solve the generalized eigenvalue equation directly.

B Training details

In this section, we provide the details of the training procedure and various hyperparameters used. We have taken $z_{max} = 10$ and $h = 0.1$, which gives $N = 100$ discretization points. The a and b values in Eq. 24 are taken as 0.01 GeV^3 and 0.03 GeV^3 respectively.

For the neural networks used to approximate $A(z)$ and $v(z)$, we employed a fully connected feedforward network with four hidden layers, each containing 50 neurons. The input layer has one neuron (representing the variable z), and the output layer also has one neuron (representing either $A(z)$ or $v(z)$). The input is scaled by dividing by z_{max} to ensure it lies within the range $[0, 1]$. We have used the SiLU (Swish) activation function [50], and the weights are initialized using the Kaiming normal initialization method [51] with leaky-ReLU.

The $\Lambda_{\mu,n}$ corresponding to the weightage of each meson mass in the loss function, which are adaptively chosen based on current loss values. The weightage is defined as,

$$\Lambda_{\mu,n} = \frac{E_{\mu,n}}{\sum_{\mu \in \{\rho, a_1, a_2, f_0\}} \sum_{i=1}^{N_\mu} E_{\mu,i}}, \quad (49)$$

where, $E_{\mu,n}$ is the error for the n^{th} mass of the meson as given in Eq. 30. Note that $\Lambda_{\mu,n}$ needs to be detached from the computational graph while calculating the loss to avoid any unwanted gradients. Additionally we have chosen $\Lambda_{v'} = 10$, $\Lambda_A = 1$ and $\Lambda_{pot} = 1$ for the other loss components given in Eq. 36.

The initial value of the model parameters l and θ are taken as 1.0 GeV^{-1} and 0.0 respectively. To find a good initial guess for the parameters k_1 and k_2 , we employ a Bayesian optimization-based Tree-Structured Parzen Estimator (TPE) [45]. We use the `Optuna` library [46] to perform the optimization. The objective function for the optimization is defined as

$$\mathcal{O}(k_1, k_2) = \sum_{\mu \in \{\rho, a_1, a_2, f_0, \pi\}} \left(\frac{1}{N_\mu} \sum_{n=1}^{N_\mu} E_{\mu,n} \right). \quad (50)$$

We define a search space for the initial value of k_1 and k_2 as $[-15, 15]$ and run the optimization for 100 trials. In each trial, we train the model for 15,000 iterations. The best values of k_1 and k_2 obtained from the optimization are $k_1 = -7.4$ and $k_2 = 12.2$. These values are used as the initial guess for k_1 and k_2 in the subsequent training runs.

To compute the loss $\mathcal{L}_{v'}$ given in Eq. 33, we choose 100 random points in the domain $z \in [0, z_{max}]$. For the loss \mathcal{L}_{pot} given in Eq. 34, we select one random point every iteration in the domain $z \in [0.8z_{max}, z_{max}]$ to enforce the asymptotic behavior of the potential.

For the training, we have used two Adam optimizers [52] with different learning rates. The first Adam optimizer is used to update the weights and biases of the neural network, with an initial learning rate of 5×10^{-4} , which is reduced in further iterations using a learning rate scheduler. The learning rate scheduler reduces the learning rate by a factor of 0.95 if the loss does not decrease for 100 iterations. The minimum learning rate is set to 10^{-8} for this optimizer. The second Adam optimizer is used to train the model parameters k_1 , k_2 , L , and θ , with an initial learning rate of 5×10^{-2} , along with a learning rate scheduler that reduces the learning rate by a factor of 0.6 if the loss does not decrease for 200 iterations. The minimum learning rate is set to 10^{-5} for this optimizer.

We have also implemented gradient clipping for all the parameters with a maximum norm of 1.0. Additionally, we have used double precision (float64) for better numerical stability. We train the model for 15,000 iterations.

We run the training multiple times and choose only those runs where the minimum total loss converges to a value below 10^{-2} . The loss curve for a representative run is shown in Fig. 6. The training loss

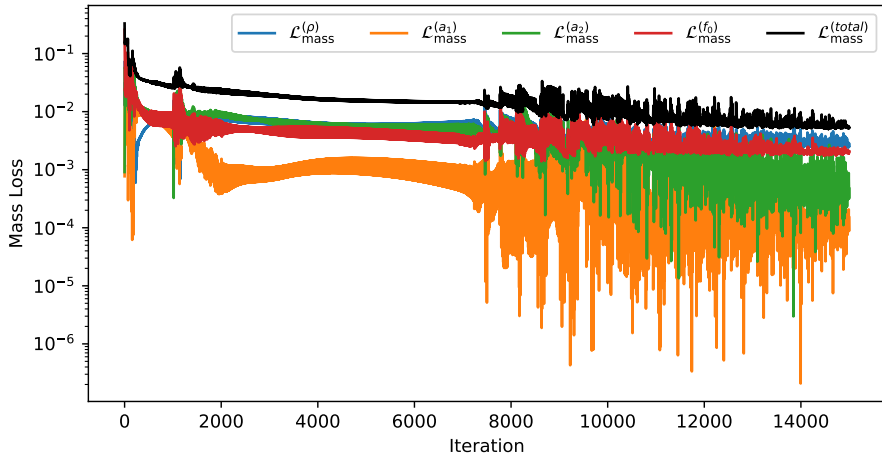


Figure 6: The loss curve for a representative training run.

Run	$\min(\mathcal{L}_{\text{mass}}^{(\rho, a_1, a_2, f_0)})$	$\mathcal{L}_{\text{mass}}^{(\pi)}$	k_1	k_2	$L \text{ (GeV)}^{-1}$	θ
1	8.59×10^{-3}	0.274	-7.39	16.26	1.49	2.97
2	9.56×10^{-3}	0.567	-7.19	15.44	1.83	1.40
3	8.24×10^{-3}	1.323	-7.34	16.10	1.70	-0.20
4	7.90×10^{-3}	0.374	-7.00	14.58	1.54	2.67
5	6.56×10^{-3}	0.431	-7.50	15.47	1.57	2.55
6	8.72×10^{-3}	0.268	-6.30	13.55	1.61	4.02
7	7.61×10^{-3}	0.610	-7.55	16.82	1.59	0.91
8	8.82×10^{-3}	0.359	-8.11	18.72	1.53	2.49
9	5.00×10^{-3}	0.455	-9.85	21.28	1.75	4.42
10	9.53×10^{-3}	0.833	-9.51	22.52	2.44	2.85

Table 5: Comparison of the minimum training loss for $\mathcal{L}_{\text{mass}}^{(\rho, a_1, a_2, f_0)}$ and the π mass loss $\mathcal{L}_{\text{mass}}^{(\pi)}$ across all runs, along with the corresponding model parameters (k_1, k_2, L, θ). Run 9 achieved the lowest training loss $\mathcal{L}_{\text{mass}}^{(\rho, a_1, a_2, f_0)}$ (This loss is weighted according to their appropriate Λ values given by the Eq. 49), while Run 6 yielded the lowest π mass loss $\mathcal{L}_{\text{mass}}^{(\pi)}$ (This loss is unweighted i.e. $\Lambda_{\pi, n} = 1$), despite not being trained for it.

for each run is given in Table 5. We trained the model on an Intel Xeon W-2245 CPU (3.90 GHz, 16 GB RAM), which took less than 30 minutes per run.

References

- [1] J. M. Maldacena, *The Large N limit of superconformal field theories and supergravity*, *Adv. Theor. Math. Phys.* **2** (1998) 231–252, [[hep-th/9711200](#)].
- [2] S. S. Gubser, I. R. Klebanov and A. M. Polyakov, *Gauge theory correlators from noncritical string theory*, *Phys. Lett. B* **428** (1998) 105–114, [[hep-th/9802109](#)].

- [3] E. Witten, *Anti de Sitter space and holography*, *Adv. Theor. Math. Phys.* **2** (1998) 253–291, [[hep-th/9802150](#)].
- [4] T. Sakai and S. Sugimoto, *Low energy hadron physics in holographic QCD*, *Prog. Theor. Phys.* **113** (2005) 843–882, [[hep-th/0412141](#)].
- [5] T. Sakai and S. Sugimoto, *More on a holographic dual of QCD*, *Prog. Theor. Phys.* **114** (2005) 1083–1118, [[hep-th/0507073](#)].
- [6] M. Kruczenski, D. Mateos, R. C. Myers and D. J. Winters, *Towards a holographic dual of large $N(c)$ QCD*, *JHEP* **05** (2004) 041, [[hep-th/0311270](#)].
- [7] K. Hashimoto, T. Hirayama, F.-L. Lin and H.-U. Yee, *Quark Mass Deformation of Holographic Massless QCD*, *JHEP* **07** (2008) 089, [[0803.4192](#)].
- [8] B. Holdom and M. E. Peskin, *Raising the Axion Mass*, *Nucl. Phys. B* **208** (1982) 397–412.
- [9] B. Holdom, *Strong QCD at High-energies and a Heavy Axion*, *Phys. Lett. B* **154** (1985) 316. [Erratum: *Phys.Lett.B* 156, 452 (1985)].
- [10] J. Erlich, E. Katz, D. T. Son and M. A. Stephanov, *Qcd and a holographic model of hadrons*, *Physical Review Letters* **95** (Dec., 2005) .
- [11] J. Hirn, N. Rius and V. Sanz, *Geometric approach to condensates in holographic QCD*, *Phys. Rev. D* **73** (2006) 085005, [[hep-ph/0512240](#)].
- [12] A. Karch, E. Katz, D. T. Son and M. A. Stephanov, *Linear confinement and AdS/QCD* , *Phys. Rev. D* **74** (2006) 015005, [[hep-ph/0602229](#)].
- [13] C. Csaki and M. Reece, *Toward a systematic holographic QCD: A Braneless approach*, *JHEP* **05** (2007) 062, [[hep-ph/0608266](#)].
- [14] A. Falkowski and M. Perez-Victoria, *Holography, pade approximants and deconstruction*, *JHEP* **02** (2007) 086, [[hep-ph/0610326](#)].
- [15] J. P. Shock, F. Wu, Y.-L. Wu and Z.-F. Xie, *AdS/QCD Phenomenological Models from a Back-Reacted Geometry*, *JHEP* **03** (2007) 064, [[hep-ph/0611227](#)].
- [16] A. Karch, E. Katz, D. T. Son and M. A. Stephanov, *On the sign of the dilaton in the soft wall models*, *JHEP* **04** (2011) 066, [[1012.4813](#)].
- [17] T. Gherghetta, J. I. Kapusta and T. M. Kelley, *Chiral symmetry breaking in the soft-wall ads/qcd model*, *Physical Review D* **79** (Apr., 2009) .
- [18] P. Zhang, *Mesons and nucleons in soft-wall ads/qcd*, *Physical Review D* **82** (Nov., 2010) .
- [19] Y.-Q. Sui, Y.-L. Wu, Z.-F. Xie and Y.-B. Yang, *Prediction for the mass spectra of resonance mesons in the soft-wall ads/qcd model with a modified 5d metric*, *Phys. Rev. D* **81** (Jan, 2010) 014024.
- [20] H. Xie, J.-G. Liu and L. Wang, *Automatic differentiation of dominant eigensolver and its applications in quantum physics*, *Phys. Rev. B* **101** (Jun, 2020) 245139.
- [21] W. de Paula, T. Frederico, H. Forkel and M. Beyer, *Dynamical holographic qcd with area-law confinement and linear regge trajectories*, *Phys. Rev. D* **79** (Apr, 2009) 075019.

- [22] A. Ballon-Bayona, T. Frederico, L. A. H. Mamani and W. de Paula, *Dynamical holographic qcd model for spontaneous chiral symmetry breaking and confinement*, *Phys. Rev. D* **108** (Nov, 2023) 106016.
- [23] L. A. H. Mamani, *Conformal symmetry breaking in holographic qcd*, *Phys. Rev. D* **100** (Nov, 2019) 106009.
- [24] K. Hornik, M. Stinchcombe and H. White, *Multilayer feedforward networks are universal approximators*, *Neural Networks* **2** (1989) 359–366.
- [25] K. Hashimoto, *AdS/CFT correspondence as a deep Boltzmann machine*, *Phys. Rev. D* **99** (2019) 106017, [[1903.04951](#)].
- [26] K. Hashimoto, S. Sugishita, A. Tanaka and A. Tomiya, *Deep Learning and Holographic QCD*, *Phys. Rev. D* **98** (2018) 106014, [[1809.10536](#)].
- [27] T. Akutagawa, K. Hashimoto and T. Sumimoto, *Deep learning and ads/qcd*, *Physical Review D* **102** (July, 2020) .
- [28] K. Hashimoto, K. Ohashi and T. Sumimoto, *Deriving the dilaton potential in improved holographic QCD from the meson spectrum*, *Phys. Rev. D* **105** (2022) 106008, [[2108.08091](#)].
- [29] R. Pal, *Github*, <https://github.com/rp-winter/NN-AdS-QCD> (2025) .
- [30] N. Arkani-Hamed, A. G. Cohen and H. Georgi, *(De)constructing dimensions*, *Phys. Rev. Lett.* **86** (2001) 4757–4761, [[hep-th/0104005](#)].
- [31] H.-C. Cheng, C. T. Hill and J. Wang, *Dynamical Electroweak Breaking and Latticized Extra Dimensions*, *Phys. Rev. D* **64** (2001) 095003, [[hep-ph/0105323](#)].
- [32] H. Abe, T. Kobayashi, N. Maru and K. Yoshioka, *Field localization in warped gauge theories*, *Phys. Rev. D* **67** (2003) 045019, [[hep-ph/0205344](#)].
- [33] L. Randall, Y. Shadmi and N. Weiner, *Deconstruction and gauge theories in AdS(5)*, *JHEP* **01** (2003) 055, [[hep-th/0208120](#)].
- [34] A. Falkowski and H. D. Kim, *Running of gauge couplings in AdS(5) via deconstruction*, *JHEP* **08** (2002) 052, [[hep-ph/0208058](#)].
- [35] D. T. Son and M. A. Stephanov, *QCD and dimensional deconstruction*, *Phys. Rev. D* **69** (2004) 065020, [[hep-ph/0304182](#)].
- [36] J. de Blas, A. Falkowski, M. Perez-Victoria and S. Pokorski, *Tools for deconstructing gauge theories in AdS(5)*, *JHEP* **08** (2006) 061, [[hep-th/0605150](#)].
- [37] J. Erlich, G. D. Kribs and I. Low, *Emerging holography*, *Phys. Rev. D* **73** (2006) 096001, [[hep-th/0602110](#)].
- [38] Y. Nakai, *Deconstruction, Holography and Emergent Supersymmetry*, *JHEP* **03** (2015) 101, [[1412.3486](#)].
- [39] E. Kiritsis and F. Nitti, *On massless 4d gravitons from asymptotically ads5 space-times*, *Nuclear Physics B* **772** (2007) 67–102.
- [40] K. Chelabi, Z. Fang, M. Huang, D. Li and Y.-L. Wu, *Chiral phase transition in the soft-wall model of ads/qcd*, *Journal of High Energy Physics* **2016** (Apr., 2016) 1–30.

- [41] U. Gürsoy and E. Kiritsis, *Exploring improved holographic theories for qcd: part i*, *Journal of High Energy Physics* **2008** (feb, 2008) 032.
- [42] A. Cherman, T. D. Cohen and E. S. Werbos, *Chiral condensate in holographic models of qcd*, *Phys. Rev. C* **79** (Apr, 2009) 045203.
- [43] T. M. Kelley, S. P. Bartz and J. I. Kapusta, *Pseudoscalar mass spectrum in a soft-wall model of ads/qcd*, *Phys. Rev. D* **83** (Jan, 2011) 016002.
- [44] A. Ballon-Bayona and L. A. H. Mamani, *Nonlinear realization of chiral symmetry breaking in holographic soft wall models*, *Phys. Rev. D* **102** (Jul, 2020) 026013.
- [45] Y. Ozaki, Y. Tanigaki, S. Watanabe and M. Onishi, *Multiobjective tree-structured parzen estimator for computationally expensive optimization problems*, in *Proceedings of the 2020 Genetic and Evolutionary Computation Conference*, GECCO '20, (New York, NY, USA), p. 533–541, Association for Computing Machinery, 2020. [DOI](#).
- [46] T. Akiba, S. Sano, T. Yanase, T. Ohta and M. Koyama, *Optuna: A next-generation hyperparameter optimization framework*, in *Proceedings of the 25th ACM SIGKDD International Conference on Knowledge Discovery and Data Mining*, 2019.
- [47] **Particle Data Group** collaboration, S. Navas et al., *Review of particle physics*, *Phys. Rev. D* **110** (2024) 030001.
- [48] K. Hashimoto, S. Sugishita, A. Tanaka and A. Tomiya, *Deep learning and the AdS/CFT correspondence*, *Phys. Rev. D* **98** (Aug, 2018) 046019.
- [49] R. P. Feynman, *Forces in molecules*, *Phys. Rev.* **56** (Aug, 1939) 340–343.
- [50] P. Ramachandran, B. Zoph and Q. V. Le, *Searching for activation functions*, 2017.
- [51] K. He, X. Zhang, S. Ren and J. Sun, *Delving deep into rectifiers: Surpassing human-level performance on imagenet classification*, 2015.
- [52] D. P. Kingma and J. Ba, *Adam: A method for stochastic optimization*, 2017.